

Robustness of error-suppressing entangling gates in cavity-coupled transmon qubits

Xiu-Hao Deng, Edwin Barnes, and Sophia E. Economou
Department of Physics, Virginia Tech, Blacksburg, Virginia 24061, USA

Superconducting transmon qubits comprise one of the most promising platforms for quantum information processing due to their long coherence times and to their scalability into larger qubit networks. However, their weakly anharmonic spectrum leads to spectral crowding in multiqubit systems, making it challenging to implement fast, high-fidelity gates while avoiding leakage errors. To address this challenge, we use a protocol known as SWIPHT [Phys. Rev. B 91, 161405(R) (2015)], which yields smooth, simple microwave pulses designed to suppress leakage without sacrificing gate speed through spectral selectivity. Here, we determine the parameter regimes in which SWIPHT is effective and demonstrate that in these regimes it systematically produces two-qubit gate fidelities for cavity-coupled transmons in the range 99.6%-99.9% with gate times as fast as 23 ns. Our results are obtained from full numerical simulations that include current experimental levels of relaxation and dephasing. These high fidelities persist over a wide range of system parameters that encompass many current experimental setups and are insensitive to small parameter variations and pulse imperfections.

PACS numbers: 03.67.Lx 03.67.Bg 85.25.Cp

I. INTRODUCTION

Rapid progress in the coherence and control of superconducting qubits over the past decade has made them a frontrunner in the quest for viable quantum computing platforms.¹⁻⁴ High fidelity single- and multi-qubit operations,⁵⁻⁹ as well as initial demonstrations of algorithms and error-correcting codes,¹⁰⁻¹⁴ have been implemented in several multi-qubit devices, and coherence times on the order of several tens of microseconds and above are now achieved regularly.¹⁵⁻²⁰ Perhaps the most promising of these are transmon qubits, in which insensitivity to charge noise is achieved by reducing the capacitive energy relative to the Josephson energy through the use of a large shunt capacitor, leading to a flattening of the charge dispersion of the energy levels.²¹⁻²³

There are two general approaches to implementing two-qubit gates in superconducting qubits. For tunable qubits such as 2D transmons²¹ or Xmons,²³ DC magnetic fields are used to set qubit energies and other circuit parameters. In many systems, such fields are also used to implement gates by temporarily bringing the system to a special parameter regime (e.g., a two-qubit resonance), where it is held idle until different states accumulate the relative phases appropriate for a desired operation.²⁴⁻²⁶ The main disadvantage of this approach is the reliance on flux-tunable qubits, which can have reduced coherence times due to flux noise.²⁷

The second general approach to gate implementation is to drive one or more qubits with modulated AC microwave pulses. This method leads to less noise since the qubit energies are held fixed, and it is the only option for systems with non-tunable qubits.²⁸⁻³⁵ The primary challenge with this approach stems from spectral crowding: a system of several coupled, weakly anharmonic qubits such as transmons possesses a dense energy spectrum with many closely spaced transitions. Faster gates are generally preferred since they allow for

faster algorithms. However, faster pulses have broader bandwidth and can thus lead to the unintended excitation of transitions that are nearly degenerate with the target transition(s), causing phase and leakage errors. On the other hand, using spectrally narrower, slower pulses to avoid this problem increases exposure to relaxation and decoherence. To date, there have been several works that address this problem in the context of single-qubit gates by devising pulses that avoid the harmful transitions, either by numerical pulse shaping³⁶ or by engineering the pulse spectrum to contain sharp holes at the frequencies of the unwanted transitions.³⁷⁻⁴¹ Recent experiments implementing microwave-driven two-qubit entangling gates in transmon devices have reported gate times and fidelities ranging from 300 – 500 ns and 87 – 97%.^{6,13,17} While there has been recent progress in designing fast leakage-suppressing two-qubit gates using numerical pulse shaping,⁴² there remains a need for fast high-fidelity gates based on simple pulses.

Instead of attempting to avoid harmful unwanted transitions, two of us proposed a new protocol called SWIPHT⁴³ to achieve fast, high-fidelity two-qubit gates by purposely driving the nearest harmful transition such that the corresponding subspace undergoes trivial cyclic evolution. This minimizes leakage errors and significantly enhances gate fidelities without resorting to slow, spectrally selective pulses. While Ref. 43 demonstrated the efficacy of SWIPHT for a set of typical parameters, a full examination of its regime of validity and its robustness to parameter variations and decoherence and relaxation has yet to be carried out.

In this paper, we fill this gap by providing a detailed investigation of the robustness of the SWIPHT protocol for two-qubit CNOT gates. We show that there exist wide fidelity plateaus in the qubit-frequency landscape where the fidelity remains above 99.9%. We also find that with our method, we are able to maintain the CNOT fidelity at 99.9% while decreasing the gate time to tens

of nano-seconds by exploiting resonances between ground and excited state transitions. We further demonstrate the robustness of these results to decoherence and relaxation, variations in qubit-cavity couplings and qubit frequencies, and pulse deformations using experimentally realistic decay times and parameter uncertainties.

II. ANALYTICAL APPROACH TO GATE DESIGN

We consider two transmons coupled to a superconducting cavity. The Hamiltonian of this system is

$$H_0 = \omega_c a^\dagger a + \sum_{\ell=1,2} [\omega_\ell b_\ell^\dagger b_\ell + \frac{\alpha_\ell}{2} b_\ell^\dagger b_\ell (b_\ell^\dagger b_\ell - 1) + g_\ell (a^\dagger b_\ell + a b_\ell^\dagger)]. \quad (1)$$

Here $a^\dagger(a)$, $b_{1,2}^\dagger(b_{1,2})$ are creation (annihilation) operators for the cavity and transmons, respectively, $\omega_{1,2}$ denote the energy splittings between the lowest two states of each transmon, $\alpha_{1,2}$ are the anharmonicities, and $g_{1,2}$ are the coupling strengths between each transmon and the cavity. Working in the Fock basis $\{|n, i, j\rangle\}$, where n is the number of cavity photons, and i, j denote the energy levels of transmon 1 and 2, respectively, we diagonalize H_0 to obtain the dressed eigenstates. In the dispersive regime and with $g_{1,2} \ll \{\omega_c, \omega_{1,2}\}$, each dressed state has a large overlap with one of the bare Fock states; hence, we use n, i, j to denote the dressed states, but with an additional tilde: $\{|\widetilde{n, i, j}\rangle\}$.

We define our computational two-qubit states to be the dressed states $\{|\widetilde{000}\rangle, |\widetilde{001}\rangle, |\widetilde{010}\rangle, |\widetilde{011}\rangle\}$, which are very close to the bare states, $\{|000\rangle, |001\rangle, |010\rangle, |011\rangle\}$, for typical system parameters. The splittings between the bare states $|000\rangle, |001\rangle$ and between $|010\rangle, |011\rangle$ are equal, as are those between $|000\rangle, |010\rangle$ and between $|001\rangle, |011\rangle$. These degeneracies are slightly broken in the dressed states due to the finite couplings $g_{1,2}$, allowing one to perform two-qubit entangling gates by driving only one transition, e.g., driving the $|\widetilde{000}\rangle \Leftrightarrow |\widetilde{010}\rangle$ transition can implement a CNOT gate:

$$\begin{aligned} \text{CNOT} = & e^{i\phi_a} |\widetilde{000}\rangle \langle \widetilde{010}| + e^{i\phi_b} |\widetilde{010}\rangle \langle \widetilde{000}| \\ & + e^{i\phi_c} |\widetilde{001}\rangle \langle \widetilde{001}| + e^{i\phi_d} |\widetilde{011}\rangle \langle \widetilde{011}|. \end{aligned} \quad (2)$$

Here, we generalize the standard CNOT by including arbitrary phases ϕ_μ ; this generalized CNOT is maximally entangling and is locally equivalent to the standard CNOT. In particular, the two are related by single-qubit Z gates, which have recently been experimentally demonstrated for fixed-frequency qubits.^{44,45}

The CNOT gate in Eq. (2) can be implemented by driving only the first transmon with a microwave π -pulse that is resonant with the $|\widetilde{000}\rangle \Leftrightarrow |\widetilde{010}\rangle$ transition. The total Hamiltonian can be written in the bare eigenbasis as

$$\mathcal{H}(t) = H_0 + b_1 \Omega(t) e^{i\omega_p t} + b_1^\dagger \Omega(t) e^{-i\omega_p t}, \quad (3)$$

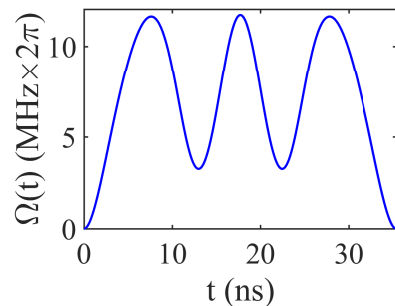


FIG. 1: Pulse envelope from Ref. 43 that implements a CNOT gate in 35.4 ns with $\omega_1 = 6.2$ GHz, $\omega_2 = 6.8$ GHz, $\omega_c = 7.15$ GHz, $\alpha_{1,2} = 350$ MHz, $g_{1,2} = 250$ MHz.

where $\Omega(t)$ and ω_p are the pulse envelope and frequency, respectively. In the dispersive regime, the simplest way to ensure that this transition is the only one excited by the pulse is to use a very narrowband pulse—an approach which necessarily leads to long gate times. To avoid making this sacrifice in gate speed, we instead employ the SWIPHT method^{43,46} to remove the effects of inadvertently driving unwanted transitions without resorting to spectrally narrow, slow pulses. For typical experimental values of the qubit-cavity couplings $g_{1,2}$, there is exactly one nearest “harmful” transition, namely the $|\widetilde{001}\rangle \Leftrightarrow |\widetilde{011}\rangle$ transition, which competes with the target transition, $|\widetilde{000}\rangle \Leftrightarrow |\widetilde{010}\rangle$. The SWIPHT protocol calls for purposely driving this transition in such a way that the net evolution operator in this subspace is proportional to an identity operation.

In the computational two-qubit subspace spanned by the states $|\widetilde{000}\rangle, |\widetilde{010}\rangle, |\widetilde{001}\rangle, |\widetilde{011}\rangle$ (note the unconventional basis ordering), the Hamiltonian of the driven transmon-cavity system is approximately

$$H_{cs} \approx \begin{pmatrix} -E/2 - \epsilon & \Omega(t)e^{i\omega_p t} & 0 & 0 \\ \Omega(t)e^{-i\omega_p t} & E/2 - \epsilon & 0 & 0 \\ 0 & 0 & -(E - \delta)/2 & \Omega(t)e^{i\omega_p t} \\ 0 & 0 & \Omega(t)e^{-i\omega_p t} & (E - \delta)/2 \end{pmatrix},$$

where E is the energy splitting between $|\widetilde{000}\rangle$ and $|\widetilde{010}\rangle$, and $E - \delta$ is the splitting between $|\widetilde{001}\rangle$ and $|\widetilde{011}\rangle$. We have shifted the overall energy by $-E/2 - \epsilon$, where $\epsilon + \delta/2$ is the energy of state $|\widetilde{001}\rangle$. We denote the pulse duration by τ_p . We have also neglected the subleading terms in the off-diagonal 2×2 blocks (but not in the simulations). To implement a SWIPHT CNOT gate, we set $\omega_p = E$ and engineer $\Omega(t)$ such that the evolution operator generated by H_{cs} coincides with the CNOT gate given in Eq. (2) with $\phi_\mu = 0$. Matching the form of the upper left 2×2 subspace requires the area of the pulse to be given by $\int_0^{\tau_p} dt \Omega(t) = \pi/2$, as is consistent with a π -pulse.

Engineering the evolution operator in the lower right 2×2 subspace to be an identity operation at time $t = \tau_p$ is more challenging since it is not possible to analytically solve the Schrödinger equation for an off-resonant

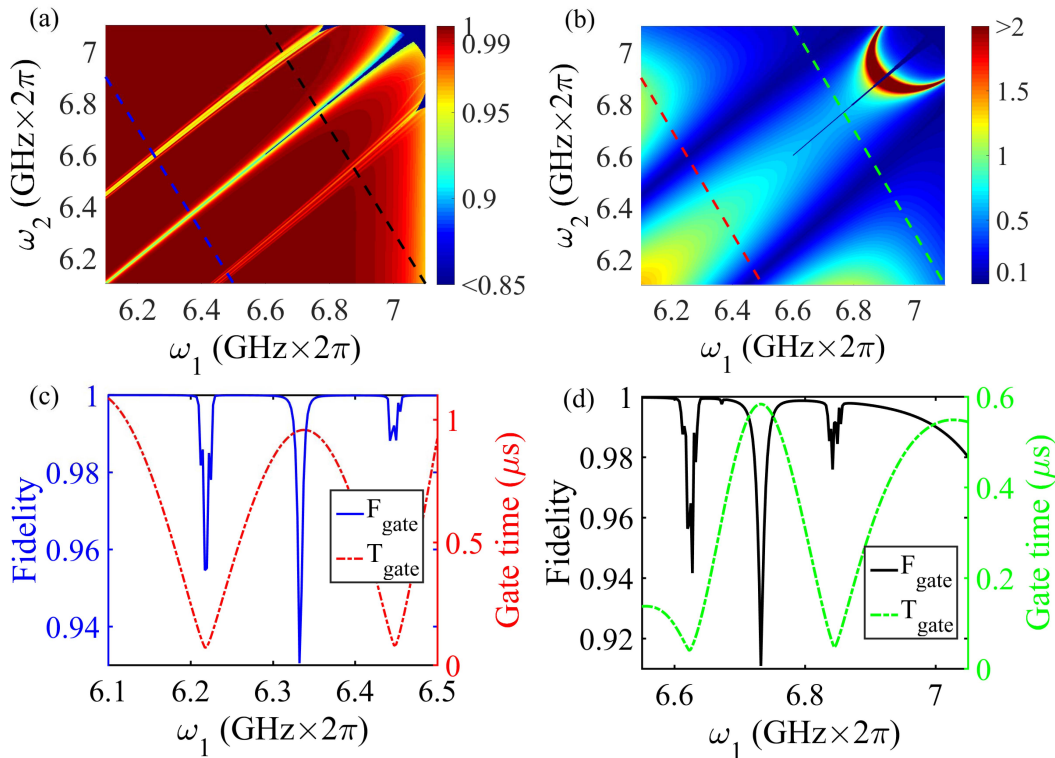


FIG. 2: (a) CNOT fidelity and (b) gate time (μs) versus qubit frequencies. $g_{1,2} = 100$ MHz, while all other parameters are as in Fig. 1. Cross-section plots for the four dashed lines are shown in (c) and (d) with corresponding colors.

pulse with arbitrary envelope $\Omega(t)$. We can overcome this difficulty by making use of a partial-reverse engineering formalism introduced in Refs. 47,48. In Ref. 43, this formalism was used to obtain the pulse shown in Fig. 1, which implements a CNOT gate with fidelity $> 99\%$ in 35.4 ns. A brief review of the construction of this pulse is given in Appendix A. The duration of the pulse is given by $\tau_p = 5.87/|\Delta|$, where $\Delta = \omega_p - (E - \delta)$ is the detuning of the pulse relative to the harmful transition. For $\omega_p = E$ we have $\Delta = \delta$, and thus τ_p depends on the system parameters through the dependence on the transition frequency difference δ , which is due to the cavity-mediated coupling. For the parameters considered in Ref. 43 (summarized in the caption of Fig. 1), $\delta = 26.4$ MHz.

III. NUMERICAL RESULTS AND ROBUSTNESS

A. Dependence of gate fidelity on qubit frequencies

First, we study the dependence of the CNOT fidelity and gate speed on the transmon frequencies. For the moment, we neglect relaxation and dephasing, although these effects will be included below. In this case, we define the gate fidelity as in Ref. 49, which accounts for

leakage outside the computational two-qubit subspace:

$$\mathcal{F}^{gate} = \frac{1}{20} [\text{Tr}(MM^\dagger) + |\text{Tr}(M)|^2], \quad (4)$$

where $M = U_{ideal}U^\dagger$, and U is the actual evolution operator, while U_{ideal} is the target gate operation, here taken as the CNOT gate defined in Eq. (2). We solve the time-dependent Schrödinger equation for the evolution operator generated by our analytical SWIPHT pulse keeping three cavity and four transmon states, for a total of 48 states. The number of states was increased until convergence in the results was achieved. For each set of system parameters, we optimize over the phases ϕ_μ . Our numerical results for \mathcal{F}^{gate} and τ_p are shown in Fig. 2. The most important features of Fig. 2(a) are the large plateaus where \mathcal{F}^{gate} is well above 0.999 (dark red); these occur in regions where $\omega_{1,2}$ are detuned from the three sharp linear features evident in the figure. The central feature corresponds to the qubit-qubit resonance, $\omega_1 = \omega_2$, while the two “secondary” resonances occur where $\omega_1 = \omega_2 + \alpha_1$ or $\omega_1 = \omega_2 - \alpha_2$, corresponding to the $|0\rangle \leftrightarrow |1\rangle$ transition of one qubit becoming degenerate with the $|1\rangle \leftrightarrow |2\rangle$ transition of the other. Near these resonances, additional harmful transitions become important, causing a decrease in fidelity. Further details regarding these resonances can be found in Appendix B. This figure also exhibits an asymmetry between the de-

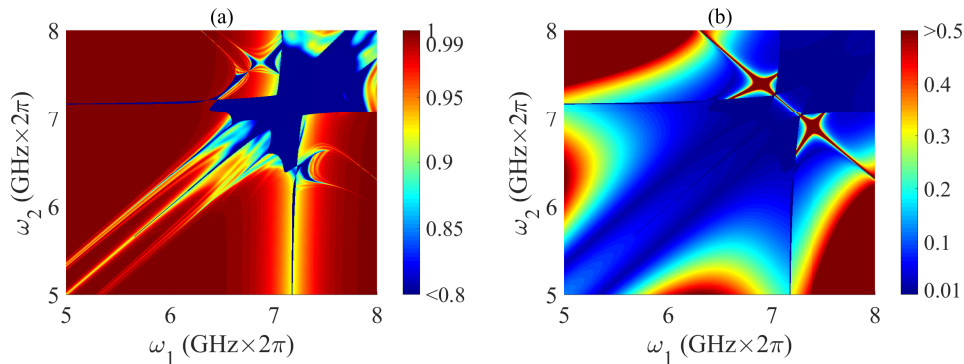


FIG. 3: CNOT fidelity (a) and gate time (μs) (b) versus qubit frequencies for $g_{1,2} = 250$ MHz.

dependencies on $\omega_{1,2}$ caused by the fact that only transmon 1 is driven. Since the high-fidelity plateau is broader for $\omega_1 < \omega_2$, we see that it is more advantageous to drive the transmon that is further detuned from the cavity.

Fig. 2(b) reveals that there is significant overlap between the high-fidelity plateaus and the parameter regions where the gate times are below 150 ns (blue). The fastest pulses occur near the secondary resonances because these give rise to a larger splitting, δ , between the target and harmful transitions, which in turn reduces the SWIPT gate time since $\tau_p \sim 1/|\delta|$. Further details can be found in Appendix B. Figs. 2(c),(d) show the CNOT fidelity and gate time along two one-dimensional slices in qubit-frequency space. Importantly, we see that while the fidelity quickly increases up to above 0.999 as ω_1 is tuned away from a secondary resonance, the gate time increases more slowly. Thus, the best combination of low gate time and high fidelity is achieved when the system lies close to a secondary resonance. From Fig. 2(d), which shows a slice closer to the cavity frequency, $\omega_c = 7.15$ GHz, we in fact see that as ω_1 is reduced, the gate time saturates at around 150 ns while the fidelity continues to improve. Below, we show that the gate time can be further reduced by more than a factor of 6 by adjusting system and pulse parameters appropriately.

Fig. 3 shows zoomed-out versions of Figs. 2(a),(b), where the full extent of the broad high-fidelity plateaus is more evident.

B. Performance under relaxation and dephasing

Next, we evaluate the impact of relaxation and decoherence on our gate by solving the Lindblad equation:

$$\dot{\rho} = i[\rho, \mathcal{H}(t)] + \sum_{\ell=1,2} \left(\frac{1}{T_1} \mathcal{D}[b_\ell] + \frac{1}{T_\phi} \mathcal{D}[b_\ell^\dagger b_\ell] \right), \quad (5)$$

with $\mathcal{D}[L] = L\rho L^\dagger - \frac{1}{2}\{L^\dagger L, \rho\}$. The first Lindblad term corresponds to qubit relaxation (time scale T_1), while the second corresponds to pure dephasing (time scale T_ϕ) caused by charge fluctuations.^{21,22} Here $1/T_2 =$

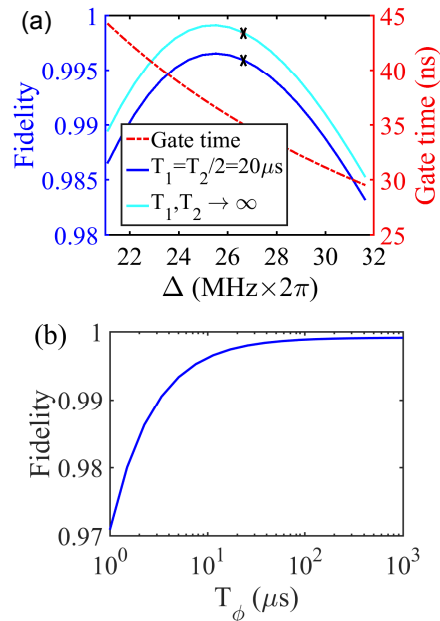


FIG. 4: (a) Fidelity versus detuning Δ for system parameters in Fig. 1. Cyan line is the fidelity for noiseless case while blue line is for $T_1 = T_2 = T_\phi/2 = 20 \mu s$. The black crosses indicate $\Delta = \delta$. Dashed red line shows gate time. (b) Average fidelity versus dephasing time T_ϕ for $\Delta = 25.5$ MHz and pulse duration is 36.6 ns, which are the optimal values found in (a).

$1/2T_1 + 1/T_\phi$. We have neglected cavity decay in our simulation because its time scale is typically much larger than T_1 and T_2 and because our gate scheme causes minimal cavity excitation. With noise terms included, \mathcal{F}^{gate} is no longer a suitable definition of fidelity, and we instead perform quantum state tomography. We prepare 16 input states in total, chosen from the set $\{|0\rangle, |1\rangle, (|0\rangle + |1\rangle)/\sqrt{2}, (|0\rangle + i|1\rangle)/\sqrt{2}\}$ for each qubit. We calculate the average fidelity, defined as $\mathcal{F} = \frac{1}{16} \sum_{j=1}^{16} \text{Tr}(\rho_{ideal}^j \rho_{sim}^j)$, where ρ_{ideal}^j is the ideal target state, while ρ_{sim}^j is the final density matrix obtained by solving Eq. (5). We again use a 48-state Hilbert space to achieve convergence and

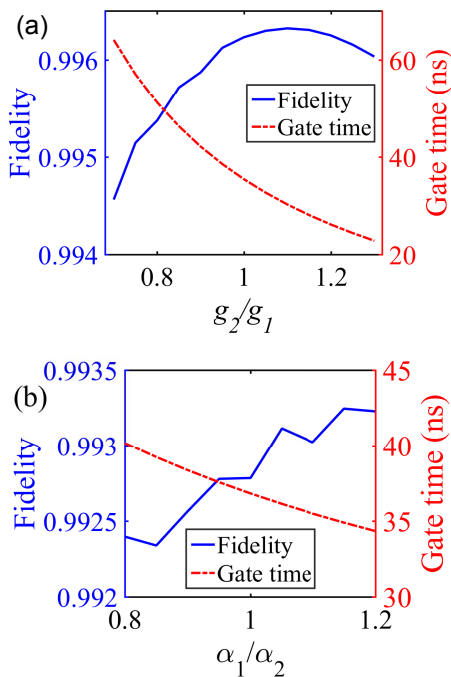


FIG. 5: (a) Fidelity and gate time versus coupling asymmetry and (b) fidelity versus anharmonicity asymmetry. The system parameters are as in Fig. 1 except as shown (g_2 and α_1 are varied), and $T_1 = T_2 = 20\mu s$.

optimize over ϕ_μ .

We first study the dependence of \mathcal{F} on the pulse detuning Δ . Fig. 4(a) shows this dependence with and without noise, where it is clear that a slight detuning away from the idealized value based on H_{cs} ($\Delta = \delta = 26.4$ MHz) down to $\Delta = 25.5$ MHz brings the fidelity up to 0.9991 without noise or up to 0.9963 with noise for typical experimental values of T_1, T_2 . The figure also shows that this improvement comes with a slight increase in the gate time from 35.4 ns up to 36.6 ns. In Fig. 4(b), we show the dependence of the fidelity on $T_\phi = 2T_1 = 2T_2$ for the optimized pulse with $\tau_p = 36.6$ ns, where we find that $\mathcal{F} \geq 0.995$ for $T_2 = T_1 \geq 7\mu s$. We also examine the performance of our gate for several sets of measured parameter values taken from recent experimental works in Appendix C. In Appendix D, we further show that the optimized local phases ϕ_μ that enter into the generalized CNOT gate (Eq. (2)) are not sensitive to experimental uncertainties in parameter values.

C. Asymmetry of coupling strength and anharmonicity

In a real setup, the qubit-cavity coupling strengths g_1, g_2 may differ. Fig. 5(a) shows that the fidelity remains > 0.995 even when the couplings differ by more than 20%. We also find that further optimization of the gate is possible if the coupling of the undriven transmon (here

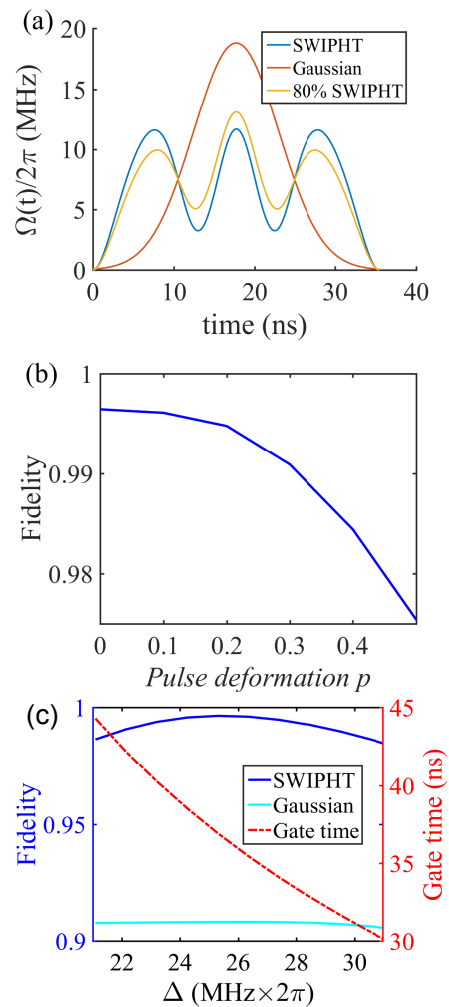


FIG. 6: (a) Pulses with Gaussian-type pulse deformations as described in Eq. (6) for three different values of the deformation parameter: $p = 0$ (SWIPHT), $p = 1$ (Gaussian), and $p = 0.2$ (80% SWIPHT, 20% Gaussian). (b) Fidelity versus degree of pulse deformation from Eq. (6). (c) CNOT fidelity and gate time versus detuning of the pulse relative to the harmful transition for the SWIPHT and Gaussian pulses shown in the left panel. All system and pulse parameters are as in Fig. 1 and $T_1 = T_2 = 20\mu s$.

g_2) is tuned to be slightly larger than that of the driven qubit (g_1). The figure further shows that the gate time is simultaneously reduced to as low as 23 ns while the fidelity remains above 0.996 even in the presence of relaxation and dephasing ($T_1 = T_2 = 20\mu s$).

SWIPHT is similarly robust against anharmonicity differences. So far, we assumed that both qubits share the same value of anharmonicity, $\alpha_1 = \alpha_2$, for simplicity. We have rerun the simulations shown in Fig. 3 for $\alpha_1 = 350$ MHz, $\alpha_2 = 300$ MHz. The results are essentially unchanged from those shown in Fig. 3 except for a shift in the location of one secondary resonance as follows trivially from the change in α_2 . In Fig 5(b), we show the SWIPHT CNOT gate fidelity versus asymmetry in anhar-

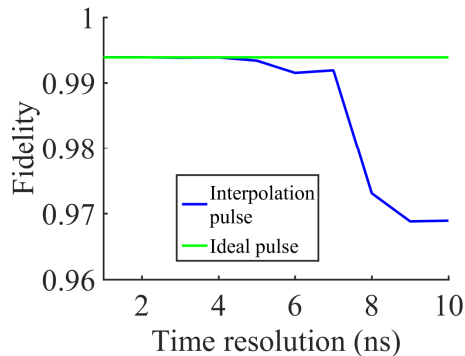


FIG. 7: Fidelity versus time resolution of pulse envelope. Pulse and system parameters are as in Fig. 1, $T_1 = T_2 = 20\mu\text{s}$.

monicity between the two transmons. It is clear from the figure that not only is the SWIPHT gate robust against anharmonicity differences, but that such differences can even lead to further improvement in the fidelity.

D. Pulse deformation

Next, we consider the robustness of the results to Gaussian-type pulse deformations of the form

$$\Omega(t) = (1 - p) * \Omega_{\text{SWIPHT}}(t) + p * \Omega_{\text{Gaussian}}(t), \quad (6)$$

where $\Omega_{\text{SWIPHT}}(t)$ is the pulse shown in Fig. 1. The Gaussian pulse, Ω_{Gaussian} , is chosen to have the same area ($\pi/2$) and duration (35.4 ns) as the SWIPHT pulse. Explicitly, we use

$$\Omega_{\text{Gaussian}}(t) = A_G e^{-(t-\tau_G/2)^2/(2\tau_G^2)}, \quad (7)$$

where $A_G = 2\pi * 18.8$ MHz, and $\tau_G = 0.15 * 35.4$ ns. The resulting pulses for three different values of p are shown in Fig. 6(a). Fig. 6(b) shows the fidelity as a function of p (with relaxation and dephasing included), where it is evident that the gate performance is essentially unchanged for deformations up to the 10% level, further highlighting the robustness of our gate. In Fig. 6(c), we show a comparison of the SWIPHT and pure Gaussian pulses; we see that the SWIPHT pulse performs dramatically better for gate times on the order of a few tens of nanoseconds.

Pulse deformations can also result from the finite time resolution of a pulse generator. In Fig. 7, we show the SWIPHT fidelity versus time resolution. The plateau of fidelity that persists up to 4 ns shows that SWIPHT is very robust to these pulse deformations. These findings demonstrate that SWIPHT is effective even with modest pulse-shaping capabilities.

IV. CONCLUSION

In conclusion, we have shown that the SWIPHT method can produce CNOT gates in cavity-coupled trans-

mon systems with fidelities well above 99.5% and gate times below 30 ns even when realistic levels of decoherence, relaxation, and parameter uncertainties are taken into account. In general, we find that SWIPHT performs well when the degeneracy between target and harmful transitions is strongly broken, either through strong qubit-cavity couplings, reduced qubit-cavity detunings, or transition resonances. Our work is of immediate use to ongoing experimental efforts to optimize the performance of transmon systems operated with microwave control.

Acknowledgments

We would like to thank A. Lupascu for interesting discussions and helpful comments.

Appendix A: SWIPHT pulse shape

In this appendix, we review how the analytical pulse used to implement the SWIPHT CNOT gate is derived.⁴³ As described in the main text, in order to implement this gate, we must design a pulse that implements a π rotation about x on the target transition and an identity operation on the harmful transition. The former is achieved by making the pulse resonant with the target transition and choosing the pulse area to be $\int_0^{\tau_p} dt \Omega(t) = \pi/2$. Ensuring that the harmful transition undergoes a trivial identity operation is more challenging, and we solve this problem by making use of the formalism introduced in Ref. [48] for analytically solving the time-dependent Schrödinger equation. In this formalism, analytical solutions are obtained by expressing both the evolution operator and the driving field in terms of an auxiliary function $\chi(t)$. One imposes constraints on $\chi(t)$ that ensure the desired evolution is obtained and then reads off the corresponding driving field that achieves this evolution using the formula

$$\Omega(t) = \frac{\ddot{\chi}}{2\sqrt{\frac{\Delta^2}{4} - \dot{\chi}^2}} - \sqrt{\frac{\Delta^2}{4} - \dot{\chi}^2} \cot(2\chi), \quad (A1)$$

where Δ is the detuning of the pulse relative to the harmful transition. Since the pulse is chosen to be resonant with the target transition, we have $\Delta = \delta$, where δ is the detuning between the target and harmful transitions. In Ref. [43], it was shown that achieving an identity operation on the harmful transition requires that the following conditions be satisfied: $\chi(0) = 0$, $\dot{\chi}(0) = 0$, $\chi(\tau_p) = \pi/4$, $\dot{\chi}(\tau_p) = 0$, $|\dot{\chi}(t)| \leq |\frac{\delta}{2}|$, and $\psi_{\pm}(\tau_p) = \frac{\delta\tau_p}{2}$ where $\psi_{\pm}(t) = \int_0^t dt' \sqrt{\Delta^2/4 - \dot{\chi}^2(t')} \csc[2\chi(t')] \pm \frac{1}{2} \arcsin(2\dot{\chi}(t)/\Delta)$. A choice of $\chi(t)$ satisfying these conditions was found to be

$$\chi(t) = A(t/\tau_p)^4(1 - t/\tau_p)^4 + \pi/4, \quad (A2)$$

with $A = 138.9$, and where the pulse duration is $\tau_p = 5.87/|\delta|$. The pulse shape that results from plugging Eq. (A2) into Eq. (A1) is shown in Fig. 1.

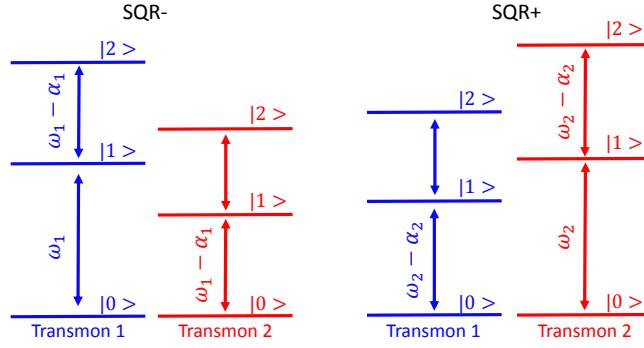


FIG. 8: Diagram of bare (non-interacting) energy levels for the two secondary qubit resonances (SQR) at which the $|0\rangle \Leftrightarrow |1\rangle$ transition of one qubit is resonant with the $|1\rangle \Leftrightarrow |2\rangle$ transition of the other. These resonances give rise to the bright linear off-diagonal features evident in Fig. 2(a).

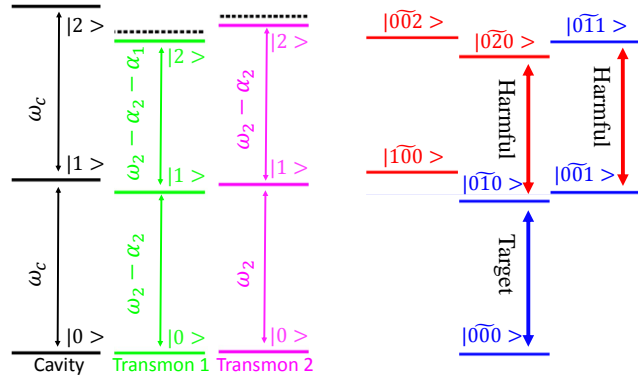


FIG. 9: Dressed state energy level diagram for the secondary qubit resonance at which the $|0\rangle \Leftrightarrow |1\rangle$ transition of qubit 2 is resonant with the $|1\rangle \Leftrightarrow |2\rangle$ transition of qubit 1, which is driven. The degeneracy between the bare states $|011\rangle$ and $|020\rangle$ at this resonance leads to a large mixing of these states when interactions are turned on, creating a large splitting between the dressed states $|\widetilde{011}\rangle$ and $|\widetilde{020}\rangle$. This in turn leads to a large detuning between the target and harmful transitions and hence a reduced gate time, which is inversely proportional to the target-harmful detuning under the SWIPHT protocol.

Appendix B: Analysis of secondary resonances

In this appendix, we provide a more detailed analysis of the secondary resonances, near which optimal gate performance can be achieved. We elucidate the origin of the gate speed-up near the secondary qubit resonances that is evident in Fig. 2. At these resonances, the $|0\rangle \Leftrightarrow |1\rangle$ transition of one qubit is resonant with the $|1\rangle \Leftrightarrow |2\rangle$ transition of the other (see Fig. 8).

For concreteness, we focus on the secondary qubit resonance at which the $|0\rangle \Leftrightarrow |1\rangle$ transition of qubit 2 is resonant with the $|1\rangle \Leftrightarrow |2\rangle$ transition of qubit 1, which is driven. The degeneracy between the bare states $|011\rangle$ and $|020\rangle$ at this resonance leads to a large mixing of these states when interactions are turned on. This gives rise to a large splitting between the dressed states $|\widetilde{011}\rangle$ and $|\widetilde{020}\rangle$, and in particular the state $|\widetilde{011}\rangle$ gets pushed to an energy that is higher than what it would be further away from the resonance (see Fig. 9). This means that the detuning between the target transition, $|\widetilde{000}\rangle \Leftrightarrow |\widetilde{010}\rangle$, and

the harmful transition, $|\widetilde{001}\rangle \Leftrightarrow |\widetilde{011}\rangle$, becomes larger. Since in the SWIPHT protocol gate time is inversely proportional to this detuning, the gate time is reduced near this secondary resonance. This is evident in Figs. 2(b-d).

Appendix C: Numerical simulations using parameters from experimental circuits

We examine the performance for several sets of parameters taken from experimental works and indicate ways to further improve results through minimal parameter adjustments. We have simulated the SWIPHT CNOT gate performance using parameters extracted from experimental works, including those of IBM,^{15–17} NIST,⁵⁰ Yale,¹⁸ Delft,¹⁹ ETH,²⁰ LPS,⁵⁰ as shown in the following tables. We have optimized the fidelity over the pulse frequency for each row of data. Asterisks indicate parameters that have been adjusted relative to what was used in the corresponding paper in order to improve performance. We have increased the coupling in cases where the cavity was

Reference	IBM	NIST	Yale	Yale ⁻	Delft	ETH	LPS
$\omega_c(\text{GHz}\times 2\pi)$	6.31	5.7*	7.5	7.5	6.8478	7.348	6.6
$\omega_1(\text{GHz}\times 2\pi)$	4.917	4.72	6.5*	6.5*	5.8899	6.18	5.6
$\omega_2(\text{GHz}\times 2\pi)$	5.415	5.1	6.18	6.18	6.477	7.0335	6.3
$\alpha_1, \alpha_2(\text{GHz}\times 2\pi)$	330, 330*	284	209	209	350	300*	211
$\mathbf{g}_1, \mathbf{g}_2(\text{MHz}\times 2\pi)$	250*	125	250*	250*	250*	250*	250*
$\mathbf{T}_1(\mu\text{s})$	30	20	60	15	25	1.33	24
$\mathbf{T}_2(\mu\text{s})$	13.8	20	8.4	8.4	39	0.967	41
\mathcal{F}^+	0.9936	0.9760	0.9951	0.9937	0.9942	0.8503	0.9900
$\tau_g^+(\text{ns})$	57.0389	167.5833	41.8092	41.5766	35.9051	73.1032	73.6202
$\Delta^+(\text{MHz}\times 2\pi)$	16.3790	5.5748	22.3453	22.4986	26.0197	12.7797	12.6900
\mathcal{F}^{ideal}	0.9996	0.9998	0.9981	0.9979	0.9983	0.9994	0.9987
$\tau_g^{ideal}(\text{ns})$	57.0389	172.5122	41.8092	41.5766	35.8913	83.0718	73.6202
$\Delta^{ideal}(\text{MHz}\times 2\pi)$	16.3790	-5.4155	22.3453	22.4986	25.7146	11.2462	-12.6900
$T_1^{F=0.999}(\mu\text{s})$	92.5	175.08	N/A	N/A	N/A	164.5	N/A

TABLE I: Experimental parameters and our simulation results. Numbers with asterisks indicate values that have been modified to yield improved results. Numbers in italics indicate values that were taken from other works since they were not provided in the paper. $\{\mathcal{F}^+, \tau_g^+, \Delta^+\}$ are the results for fidelity, gate time, and pulse detuning, respectively, obtained by adjusting one of the qubit frequencies for improved performance. $\{\mathcal{F}^{ideal}, \tau_g^{ideal}, \Delta^{ideal}\}$ are the results for the fidelity in the absence of relaxation and dephasing for the improved parameters. The column labeled Yale⁻ accounts for a reduction in relaxation time T_1 as a consequence of the enhancement in cavity-qubit coupling $g_{1,2}$.

Reference	IBM	IBM ^{D2Q}	NIST	NIST ^{D2Q}	Yale	Yale ^{D2Q}	Delft	Delft ^{D2Q}	ETH	ETH ^{D2Q}	LPS	LPS ^{D2Q}
$\omega_c(\text{GHz}\times 2\pi)$	6.494	6.494	6.3(5.6*)	6.3(5.6*)	7.5	7.5	6.8506	6.8506	7.347	7.347	6.6	6.6
$\omega_1(\text{GHz}\times 2\pi)$	4.917(4.72*)	4.917(4.72*)	4.72	4.72	4.87(6.5*)	6.5(6.5*)	5.8899	5.8899	6.18	6.18	5.6	5.6
$\omega_2(\text{GHz}\times 2\pi)$	5.415	5.415	5.1	5.1	6.18	6.18	6.477	6.477	7.0335	7.0335	6.3	6.3
$\alpha(\text{GHz}\times 2\pi)$	330	330	284	284	212	212	350	350	90(300*)	90(300*)	211	211
$\mathbf{g}_1, \mathbf{g}_2(\text{MHz}\times 2\pi)$	250*	250*	125	125	250*	250*	250*	250*	250*	250*	70(250*)	250*
$\mathbf{T}_1(\mu\text{s})$	30	30	20	20	60	60	25	25	1.33	1.33	24	24
$\mathbf{T}_2(\mu\text{s})$	13.8	13.8	20	20	8.4	8.4	39	39	0.967	0.967	41	41
\mathcal{F}	0.9925	0.9910	0.9293	0.9334	0.8957	0.8870	0.9942	0.9981	0.6756	0.6440	0.6430	
$\tau_g(\text{ns})$	69.5868	61.7387	511.2219	473.2454	1512.3	1498.8	35.8913	35.8913	200.6993	200.6993	4328.7	
$\Delta(\text{MHz}\times 2\pi)$	13.4255	15.1322	1.8275	1.9741	0.6177	0.6233	25.7146	26.0297	4.6549	4.6549	0.2158	
\mathcal{F}^*	0.9821	0.9828	0.9760	0.9741	0.9949	0.9555	0.9942	0.9981	0.8492	0.8586	0.9904	0.9904
$\tau_g^*(\text{ns})$	173.2139	168.9891	167.5833	186.1	41.1427	42.8220	35.8913	35.8913	72.7194	73.1099	73.6202	69.9620
$\Delta^*(\text{MHz}\times 2\pi)$	5.3936	5.5284	5.5748	5.0199	22.7073	21.8168	25.7146	26.0297	12.8472	12.7786	12.6900	13.3535
\mathcal{F}^{*ideal}	0.9999		0.9998		0.9987	0.9972	0.9983		0.9993		0.9988	0.9977
$\tau_g^{*ideal}(\text{ns})$	173.2139		172.5122		41.1427	40.8755	36.3311		83.4134		72.7289	69.9620
$\Delta^{*ideal}(\text{MHz}\times 2\pi)$	-5.3936		5.4155		22.7073	22.8557	25.7146		11.2001		12.8455	13.3535
$T_1^{F=0.999}(\mu\text{s})$	166.25		175.08		N/A		N/A		175		N/A	

TABLE II: SWIPHT CNOT gate performance in the case where both qubits are driven (D2Q) at the same time. Numbers with asterisks indicate values that have been modified to yield improved results. Numbers in italics indicate values that were taken from other works since they were not provided in the paper.

too far detuned from the qubits to yield feasible gate times within the SWIPHT scheme. In general, SWIPHT works when the degeneracy between the target and harmful transitions is strongly broken, which requires either strong qubit-cavity couplings, reduced qubit-cavity detunings, or tuning qubit parameters to lie near secondary resonances (see Appendix B). Fidelities outside the operational regime of SWIPHT are typically below 90%. Couplings up to 250 MHz are experimentally reasonable since there exist experimental filtering techniques that can enable one to increase the coupling strength without sacrificing T_1 times through Purcell effects.^{51–53} In the column labeled Yale⁻ in Table I, we show the perfor-

mance without such filtering, where the relaxation time is reduced by a factor of 4 as a consequence of the factor of 2 enhancement in qubit-cavity coupling. We see that the performance is not significantly affected provided the original relaxation time is well above 10 μs . As described in the main text and in Appendix B, we have demonstrated a way to improve the gate quality $\{\mathcal{F}^+, \tau_g^+, \Delta^+\}$ by tuning one qubit frequency so that the system lies near a secondary resonance. $\{\mathcal{F}^{ideal}, \tau_g^{ideal}, \Delta^{ideal}\}$ are the results for the fidelity (obtained from quantum state tomography) without noise for the improved parameters. In the last row, $T_{1,2}^{F=0.999}$ indicates a threshold of decoherence in order to reach a fidelity of 99.9% for a spe-

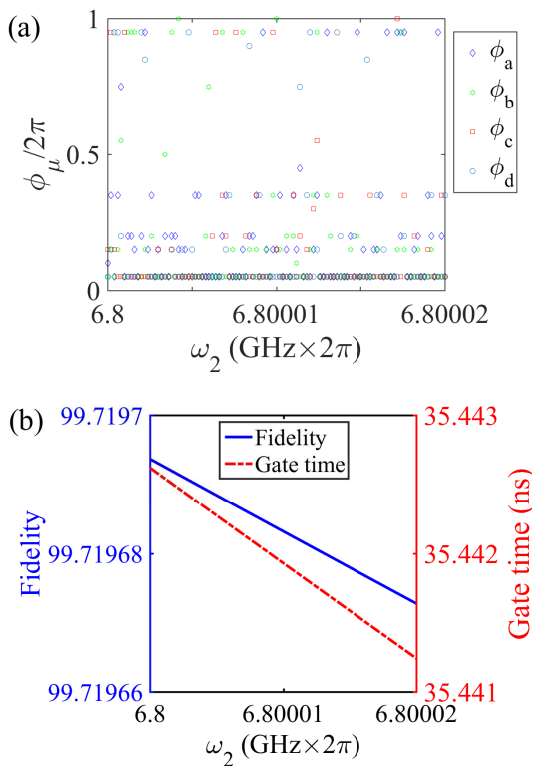


FIG. 10: (a) Local phases of the generalized CNOT as a function of qubit frequency. (b) Insensitivity of the SWIPHT gate fidelity with respect to local phases. The fidelity as a function of qubit frequency is shown for fixed values of local phases. The system parameters are as in Fig. 1 and $T_1 = T_2 = 20\mu\text{s}$.

cific set of parameters with corresponding Δ^+ . Here we

have assumed $T_1^{0.999} = T_2^{0.999}/2$. This threshold T_1 value provides an idea of the noise level needed for a specific transmon system to achieve 0.999 fidelity for a CNOT gate based on our scheme. Table I shows that it is possible to obtain fidelities in excess of 0.99 while keeping pulse times below 100 ns in most cases even with realistic noise included. The ideal fidelity values further show that most of the residual gate error is caused by decoherence and relaxation. Table II gives similar results for additional parameter sets. The table further shows that the results are essentially the same when the driving is allowed to act on both qubits.

Appendix D: Sensitivity to local phases of the generalized CNOT

We consider how the phases entering into the definition of our generalized CNOT gate, Eq. (2), depend on system parameters. These phases represent the trivial, local part of the entangling gate and can be corrected with local single-qubit gates. Due to the finite linewidths of the transmon excited states, there exists experimental uncertainty in the values of the transmon frequencies (on the order of 10 kHz), and this can in turn create uncertainty in the values of the local phases. In Fig. 10 we show that although the local phases are sensitive to qubit frequencies (Fig. 10 (a)), the SWIPHT CNOT gate fidelity remains essentially constant as qubit frequencies are varied over a range of 20 kHz even when the local phases are held fixed, demonstrating that the gate performance is not sensitive to these phases or to typical levels of uncertainty in qubit frequencies (Fig. 10 (b)).

- ¹ J. Clarke and F. K. Wilhelm, *Nature* **453**, 1031 (2008).
- ² J. Q. You and F. Nori, *Nature* **474**, 589 (2011).
- ³ M. H. Devoret and R. J. Schoelkopf, *Science* **339**, 1169 (2013).
- ⁴ J. M. Martinis and A. Megrant, arXiv:1410.5793 (2014).
- ⁵ J. M. Chow, J. M. Gambetta, A. D. Corcoles, S. T. Merkel, J. A. Smolin, C. Rigetti, S. Poletto, G. A. Keefe, M. B. Rothwell, J. R. Rozen, et al., *Phys. Rev. Lett.* **109**, 060501 (2012).
- ⁶ J. M. Chow, J. M. Gambetta, A. W. Cross, S. T. Merkel, C. Rigetti, and M. Steffen, *New J. Phys.* **15**, 115012 (2013).
- ⁷ R. Barends, J. Kelly, A. Megrant, A. Veitia, D. Sank, E. Jeffrey, T. C. White, J. Mutus, A. G. Fowler, B. Campbell, et al., *Nature* **508**, 500 (2014).
- ⁸ L. DiCarlo, M. D. Reed, L. Sun, B. R. Johnson, J. Chow, J. M. Gambetta, L. Frunzio, S. M. Girvin, M. H. Devoret, and R. J. Schoelkopf, *Nature* **467**, 574 (2010).
- ⁹ A. Fedorov, L. Steffen, M. Baur, M. P. da Silva, and A. Wallraff, *Nature* **481**, 170 (2012).
- ¹⁰ L. DiCarlo, J. M. Chow, J. M. Gambetta, L. S. Bishop, D. I. S. B. R. Johnson, J. Majer, A. Blais, L. Frunzio, S. M. Girvin, and R. J. Schoelkopf, *Nature* **460**, 240 (2009).
- ¹¹ M. Mariantoni, H. Wang, T. Yamamoto, M. Neeley, R. C. Bialczak, Y. Chen, M. Lenander, E. Lucero, A. D. OConnell, D. Sank, et al., *Science* **334**, 61 (2011).
- ¹² E. Lucero, R. Barends, Y. Chen, J. Kelly, M. Mariantoni, A. Megrant, P. O'Malley, D. Sank, A. Vainsencher, J. Wenner, et al., *Nat. Phys.* **8**, 719 (2012).
- ¹³ J. M. Chow, J. M. Gambetta, E. Magesan, S. J. Srinivasan, A. W. Cross, D. W. Abraham, N. A. Masluk, B. R. Johnson, C. A. Ryan, and M. Steffen, *Nat. Commun.* **5**, 4015 (2014).
- ¹⁴ M. D. Reed, L. DiCarlo, S. E. Nigg, L. Sun, L. Frunzio, S. M. Girvin, and R. J. Schoelkopf, *Nature* **482**, 382 (2012).
- ¹⁵ D. C. McKay, S. Filipp, A. Mezzacapo, E. Magesan, J. M. Chow, and J. M. Gambetta, *Phys. Rev. Applied* **6**, 064007 (2016).
- ¹⁶ S. Sheldon, L. S. Bishop, E. Magesan, S. Filipp, J. M. Chow, and J. M. Gambetta, *Phys. Rev. A* **93**, 012301 (2016).
- ¹⁷ A. Córcoles, E. Magesan, S. J. Srinivasan, A. W. Cross, M. Steffen, J. M. Gambetta, and J. M. Chow, *Nat. Commun.* **6**, 6979 (2015).

- ¹⁸ Y. Liu, S. Shankar, N. Ofek, M. Hatridge, A. Narla, K. Sliwa, L. Frunzio, R. J. Schoelkopf, and M. H. Devoret, *Phys. Rev. X* **6**, 011022 (2016).
- ¹⁹ C. Bultink, M. Rol, T. O'Brien, X. Fu, B. Dikken, R. Vermeulen, J. de Sterke, A. Bruno, R. Schouten, and L. DiCarlo, arXiv preprint arXiv:1604.00916 (2016).
- ²⁰ S. Berger, M. Pechal, P. Kurpiers, A. Abdumalikov, C. Eichler, J. Mlynek, A. Shnirman, Y. Gefen, A. Wallraff, and S. Filipp, *Nat. Commun.* **6** (2015).
- ²¹ J. Koch, T. M. Yu, J. Gambetta, A. A. Houck, D. I. Schuster, J. Majer, A. Blais, M. H. Devoret, S. M. Girvin, and R. J. Schoelkopf, *Phys. Rev. A* **76**, 042319 (2007).
- ²² L. S. Bishop, arXiv preprint arXiv:1007.3520 (2010).
- ²³ R. Barends, J. Kelly, A. Megrant, D. Sank, E. Jeffrey, Y. Chen, Y. Yin, B. Chiaro, J. Mutus, C. Neill, et al., *Phys. Rev. Lett.* **111**, 080502 (2013).
- ²⁴ T. Yamamoto, M. Neeley, E. Lucero, R. Bialczak, J. Kelly, M. Lenander, M. Mariantoni, A. OConnell, D. Sank, H. Wang, et al., *Phys. Rev. B* **82**, 184515 (2010).
- ²⁵ R. Bialczak, M. Ansmann, M. Hofheinz, M. Lenander, E. Lucero, M. Neeley, A. OConnell, D. Sank, H. Wang, M. Weides, et al., *Phys. Rev. Lett.* **106**, 060501 (2011).
- ²⁶ A. Dewes, F. Ong, V. Schmitt, R. Lauro, N. Boulant, P. Bertet, D. Vion, and D. Esteve, *Phys. Rev. Lett.* **108**, 057002 (2012).
- ²⁷ F. Yoshihara, K. Harrabi, A. Niskanen, Y. Nakamura, and J. Tsai, *Phys. Rev. Lett.* **97**, 167001 (2006).
- ²⁸ H. Paik, A. Mezzacapo, M. Sandberg, D. McClure, B. Abdo, A. Córcoles, O. Dial, D. Bogorin, B. Plourde, M. Steffen, et al., *Phys. Rev. Lett.* **117**, 250502 (2016).
- ²⁹ S. Poletto, J. M. Gambetta, S. T. Merkel, J. A. Smolin, J. M. Chow, A. Córcoles, G. A. Keefe, M. B. Rothwell, J. Rozen, D. Abraham, et al., *Phys. Rev. Lett.* **109**, 240505 (2012).
- ³⁰ J. M. Chow, A. Córcoles, J. M. Gambetta, C. Rigetti, B. Johnson, J. A. Smolin, J. Rozen, G. A. Keefe, M. B. Rothwell, M. B. Ketchen, et al., *Phys. Rev. Lett.* **107**, 080502 (2011).
- ³¹ P. Leek, S. Filipp, P. Maurer, M. Baur, R. Bianchetti, J. Fink, M. Göppl, L. Steffen, and A. Wallraff, *Phys. Rev. B* **79**, 180511 (2009).
- ³² J. Majer, J. M. Chow, J. M. Gambetta, J. Koch, B. R. Johnson, J. A. Schreier, L. Frunzio, D. I. Schuster, A. A. Houck, A. Wallraff, et al., *Nature* **449**, 443 (2007).
- ³³ P. De Groot, J. Lisenfeld, R. Schouten, S. Ashhab, A. Lupascu, C. Harmans, and J. Mooij, *Nat. Phys.* **6**, 763 (2010).
- ³⁴ C. Rigetti and M. Devoret, *Phys. Rev. B* **81**, 134507 (2010).
- ³⁵ P. De Groot, S. Ashhab, A. Lupascu, L. DiCarlo, F. Nori, C. Harmans, and J. Mooij, *New J. Phys.* **14**, 073038 (2012).
- ³⁶ P. Reberntrost and F. K. Wilhelm, *Phys. Rev. B* **79**, 060507(R) (2009).
- ³⁷ F. Motzoi, J. M. Gambetta, P. Reberntrost, and F. K. Wilhelm, *Phys. Rev. Lett.* **103**, 110501 (2009).
- ³⁸ J. M. Gambetta, F. Motzoi, S. T. Merkel, and F. K. Wilhelm, *Phys. Rev. A* **83**, 012308 (2011).
- ³⁹ F. Motzoi and F. K. Wilhelm, *Phys. Rev. A* **88**, 062318 (2013).
- ⁴⁰ R. Schutjens, F. A. Dagga, D. Egger, and F. Wilhelm, *Phys. Rev. A* **88**, 052330 (2013).
- ⁴¹ L. S. Theis, F. Motzoi, and F. K. Wilhelm, *Phys. Rev. A* **93**, 012324 (2016), URL <https://link.aps.org/doi/10.1103/PhysRevA.93.012324>.
- ⁴² S. Kirchhoff, T. Keßler, P. J. Liebermann, E. Assémat, S. Machnes, F. Motzoi, and F. K. Wilhelm, ArXiv e-prints (2017), 1701.01841.
- ⁴³ S. E. Economou and E. Barnes, *Phys. Rev. B* **91**, 161405 (2015).
- ⁴⁴ H. S. Ku, J. L. Long, X. Wu, M. Bal, R. E. Lake, E. Barnes, S. E. Economou, and D. P. Pappas, ArXiv e-prints (2017), 1704.00803.
- ⁴⁵ D. C. McKay, C. J. Wood, S. Sheldon, J. M. Chow, and J. M. Gambetta, ArXiv e-prints (2016), 1612.00858.
- ⁴⁶ E. Barnes, C. Arenz, A. Pitchford, and S. E. Economou, ArXiv e-prints (2016), 1612.09384.
- ⁴⁷ E. Barnes and S. Das Sarma, *Phys. Rev. Lett.* **109**, 060401 (2012).
- ⁴⁸ E. Barnes, *Phys. Rev. A* **88**, 013818 (2013).
- ⁴⁹ L. H. Pedersen, K. Molmer, and N. M. Moller, *Phys. Lett. A* **367**, 47 (2007).
- ⁵⁰ Private communication.
- ⁵¹ M. D. Reed, B. R. Johnson, A. A. Houck, L. DiCarlo, J. M. Chow, D. I. Schuster, L. Frunzio, and R. J. Schoelkopf, *Appl. Phys. Lett.* **96**, 203110 (2010).
- ⁵² J. D. Whittaker, F. C. S. da Silva, M. S. Allman, F. Lecocq, K. Cicak, A. J. Sirois, J. D. Teufel, J. Aumentado, and R. W. Simmonds, *Phys. Rev. B* **90**, 024513 (2014).
- ⁵³ N. T. Bronn, E. Magesan, N. A. Masluk, J. M. Chow, J. M. Gambetta, and M. Steffen, *IEEE Transactions on Applied Superconductivity* **25**, 1700410 (2015).